Research Article Vol. 29, No. 11 / 24 May 2021 / Optics Express 16749
Optics EXPRESS

Rapid optical tomographic vibrometry using a swept multi-gigahertz comb

SAMUEL CHOI,[1,*] TAKERU OTA,[2] FUMIAKI NIN,[3] TATSUTOSHI SHIODA,[4] TAKAMASA SUZUKI,[1] AND HIROSHI HIBINO[2]

[1]*Niigata University, Department of Electrical and Electronics Engineering, 8050 Ikarashi-2, Nishi-ward, Niigata City, Niigata 950-2181, Japan*
[2]*Osaka University, Graduate School of Medicine, Division of Glocal Pharmacology, Department of Pharmacology, 2-2 Yamadaoka, Suita, Osaka 565-0871, Japan*
[3]*Gifu University, Graduate School of Medicine, Division of Biological Principles, Department of Physiology, 1-1 Yanagido, Gifu 501-1194, Japan*
[4]*Saitama University, Graduate School of Science and Engineering, 255 Shimo-Okubo, Sakura-ward, Saitama City, Saitama 338-8570, Japan*
[*]*schoi@eng.niigata-u.ac.jp*

Abstract: We propose a rapid tomographic vibrometer technique using an optical comb to measure internal vibrations, transient phenomena, and tomographic distributions in biological tissue and microelectromechanical system devices at high frequencies. This method allows phase-sensitive tomographic measurement in the depth direction at a multi-MHz scan rate using a frequency-modulated broadband electrooptic multi-GHz supercontinuum comb. The frequency spacing was swept instantaneously in time and axisymmetrically about the center wavelength via a dual-drive Mach–Zehnder modulator driven by a variable radio frequency signal. This unique sweeping method permits direct measurement of fringe-free interferometric amplitude and phase with arbitrarily changeable measurement range and scan rate. Therefore, a compressive measurement can be made in only the depth region where the vibration exists, reducing the number of measurement points. In a proof-of-principle experiment, the interferometric amplitude and phase were investigated for in-phase and quadrature phase-shifted interferograms obtained by a polarization demodulator. Tomographic transient displacement measurements were performed using a 0.12 mm thick glass film and piezo-electric transducer oscillating at 10–100 kHz with scan rates in the range 1–20 MHz. The depth resolution and precision of the vibrometer were estimated to be approximately 25 μm and 1.0 nm, respectively.

1. Introduction

High-speed vibration phenomena are widely observed in microelectromechanical system (MEMS) oscillators and biological tissues related to hearing and bone conduction. There is increasing demand for non-invasive optical measurement technology to detect and visualize the vibration distributions of these objects along with their internal structures. In recent years, a variety of vibrometry techniques based on Doppler optical coherence tomography (OCT) [1–3] have been used to meet these requirements. In particular, Fourier domain (FD) OCT (FD-OCT) has been widely used in auditory research [4–6] to elucidate the vibration phenomena induced by sound stimulation in the sensory epithelium of the inner ear. Gao et al. measured sensory epithelial zone oscillations up to 11 kHz with a sensitivity of less than 1 nm using spectral domain (SD) OCT (SD-OCT) from the apex of an unopened mouse cochlea [4,5]. Lee et al. used swept source (SS) OCT (SS-OCT) to measure sectorial and basilar membrane traveling waves in mouse cochlea at a 200-kHz scan rate with an in vivo sensitivity to sound stimuli at Nyquist frequencies up to 100 kHz of 17 ± 8 pm [6]. Various phase-sensitive FD Doppler OCT techniques have also been used to measure vibrations in the middle ear and tympanic membrane [7–9].

#425972 https://doi.org/10.1364/OE.425972
Journal © 2021 Received 25 Mar 2021; revised 8 May 2021; accepted 10 May 2021; published 14 May 2021

Optics EXPRESS

Nevertheless, considering further applications, such as high-frequency vibration in the ultrasonic region and cross-sectional transient phenomena measurement, there is a limitation in the measurement speed (sampling rate of the image sensor for SD-OCT or scan rate of the wavelength tunable source for SS-OCT). For instance, in the case of mouse cochlea, the characteristic frequency at the basal turn, where a probe beam can be introduced noninvasively through a transparent membrane called a round window, reaches over 50 kHz [10]. In addition, ultrasonic devices, such as MEMS oscillators, vibrate at a very high frequency in the MHz band, requiring a depth scan rate of several MHz or higher. For the measurement of such ultrafast vibrating surfaces, heterodyne interference techniques with laser Doppler vibrometer microscopy [11] and time-resolved synthetic holographic confocal microscopy [12], as well as dynamic measurement of transients with STEAM [13], have been proposed. However, these ultrafast technologies were not designed to obtain cross-sectional information inside objects.

For fast tomography, various types of OCT have been developed to significantly improve the measurement speed and achieve multi-MHz scan rates [14–20]. Choi et al. developed ultrafast SD-OCT using parallel photoreceivers and an analog-to-digital (A/D) converter array to achieve a 10–60 MHz scan rate [14,15]. Wieser et al. achieved a depth scan rate of 5.2 MHz using a Fourier domain mode locked (FDML) laser and demonstrated speckle reduction by averaging [16]. Ultrafast OCT with a scan rate of 5–90.9 MHz has been achieved by time stretching using a mode-locked pulse laser and dispersive fiber [17–20]. Circular ranging OCT with a 7.6–18.9 MHz A-scan rate using a stretched pulse mode-locked (SPML) laser [21,22] and a compressive A-scan optical sampling method that can achieve a 144 MHz scan rate [23] have also been proposed. These multi-MHz OCT techniques are focused on the development of stable low-noise broadband mode-locked lasers [19], such as FDML and SPML lasers, and compression of the depth range and sampling data [21–24]. They are aimed at high-sensitivity and high-resolution Doppler OCT applications for video rate 3D or 4D OCT imaging [20] and angiography [25,26] rather than internal vibration measurement by M-scan mode.

Another existing technical issue is that it is difficult to arbitrarily adjust the measurement area in the depth direction in FD-OCT because the measurement range is fixed by the frequency resolution of the observed interference spectrum, and the targeted area is often a small fraction of the entire measurement area. For instance, the vibrating tissue of the inner ear sensory epithelium is distributed over a thickness of only 50–100 μm [6,10], whereas the typical OCT measurement range is 1–10 mm. Eliminating the wasted area that is not involved in the measurement is an important issue for compressive measurement. Therefore, a newly designed optical system is required for dynamic and transient measurements, including cross-sectional tomography or topography, with easy and alternative access to the region of interest.

To address these issues, we propose a highly advanced version of the optical comb-based interferometry technique [27–29] for fast tomographic vibration measurement. A similar technique, dual-comb interferometry [30–32], has previously been proposed, but it requires two mode-locked lasers and mechanical manipulation of the cavity length to change the repetition rate, which complicates the configuration of the light source; moreover, this technique cannot effectively utilize phase-sensitive measurements based on the carrier envelope offset (CEO) frequency of the frequency comb. As the phase sensitive methods, Boudreau et al. employed the cavity tuning method for range-resolved vibration measurements using single frequency comb [33]. Furthermore, Teleanu et al. proposed electro-optic (EO) dual-comb vibrometry to achieve sub-nanometer precision by detecting carrier phases in Fourier domain [34]. These methods, however, are based on acousto-optic modulator assisted methods measuring beat signals, thus simultaneous tomographic vibration measurement at multi-MHz scan rate has not yet been realized. Conversely, our proposed method is based on single EO broadband supercontinuum (SC) comb [35,36] generated by a dual-drive Mach Zehnder modulator (DD-MZM) [37,38] and characterized by rapid phase-sensitive tomographic depth sensing with electrically controlled

Optics EXPRESS

sampling and multi-MHz scan rate. To the best of our knowledge, this is the first time the DD-MZM has been used in this manner. The frequency spacing (FS) of the comb is swept instantaneously in time and symmetrically with respect to the center frequency (i.e., the carrier frequency component) via a non-cavity type modulator driven by a variable RF signal. This unique frequency sweeping generates an interference signal without a fringe, which is also observed as a peak envelope with a fixed phase. Because the FS and center frequency are not always integer multiples, the fixed interferometric phase takes a certain value other than 2π or 0 depending on the CEO frequency and optical path difference (OPD) of the interferometer. Furthermore, the amplitude of this fringe-free peak envelope is proportional to the cosine of the phase value [39,40]. Using this phase-sensitive interferometric characteristic, the phase and intensity distributions in the depth profile of the reflectance can be obtained simultaneously while greatly reducing the number of measurement points.

We conducted tomographic vibration measurements using the SC comb and an unbalanced interferometer as a proof-of-principle experiment to verify the proposed method. To retrieve the phase and intensity, "in-phase" and "quadrature phase shifted" signals (I- and Q-signals, respectively) were simultaneously observed using a 1/8-wave plate and polarization coupler inserted in the reference arm of the interferometer. The tomographic amplitude and phase distributions were directly derived from these I- and Q-signals. In the experiment, we measured the cross-sectional vibration of a 0.12 mm thick glass film vibrating with sound waves and a surface of a piezoelectric transducer (PZT) element vibrating at 10–100 kHz with scan rates in the range 1–20 MHz. We achieved a depth resolution of 25 μm in tomographic imaging and a sensitivity of approximately 1.0 nm at a vibration frequency of 100 kHz.

2. Method

2.1. Principle of proposed optical comb interferometry

As shown in Fig. 1, the interference signal obtained when sweeping the FS of a non-cavity-type optical comb generator with a phase modulator is expressed as the sum of the interference waveforms caused by the frequency change of each longitudinal mode of the comb. In an ideal optical comb, where each longitudinal mode can be treated as a delta function, the interference term contributed by the m-th longitudinal mode counting from its center frequencyν_0 can be written as follows:

$$I_m(f_{RF}, L_{opd}) = a_m \cos\left(\frac{2\pi(\nu_0 + mf_{RF})}{c} L_{opd}\right), \tag{1}$$

where a_m is the amplitude of the interference caused by the m-th longitudinal mode, L_{opd} is the round-trip OPD of the interferometer, f_{RF} is the frequency of the RF signal that determines the FS of the optical comb, and c denotes the speed of light. For simplicity, the noise and bias components are ignored.

The resulting interference signal generated by all frequency components of the optical comb is expressed as follows:

$$\begin{aligned} I(L_{opd}, f_{FR}) &= \sum_{m=-\infty}^{\infty} I_m(L_{opd}, f_{FR}) \\ &= a_0 \cos\left(\frac{2\pi\nu_0 L_{opd}}{c}\right) + \sum_{m=1}^{\infty}\left(a_m \cos\left(\frac{2\pi(\nu_0 + mf_{RF})L_{opd}}{c}\right) + a_m \cos\left(\frac{2\pi(\nu_0 - mf_{RF})L_{opd}}{c}\right)\right) \\ &= \cos\left(\frac{2\pi\nu_0 L_{opd}}{c}\right) \cdot \left[\sum_{m=-\infty}^{\infty}\left(a_m \cos\left(\frac{2\pi m f_{RF} L_{opd}}{c}\right)\right)\right] = B(f_{RF}, L_{OPD}) \cos\left(\frac{2\pi\nu_0 L_{opd}}{c}\right). \end{aligned} \tag{2}$$

Optics EXPRESS

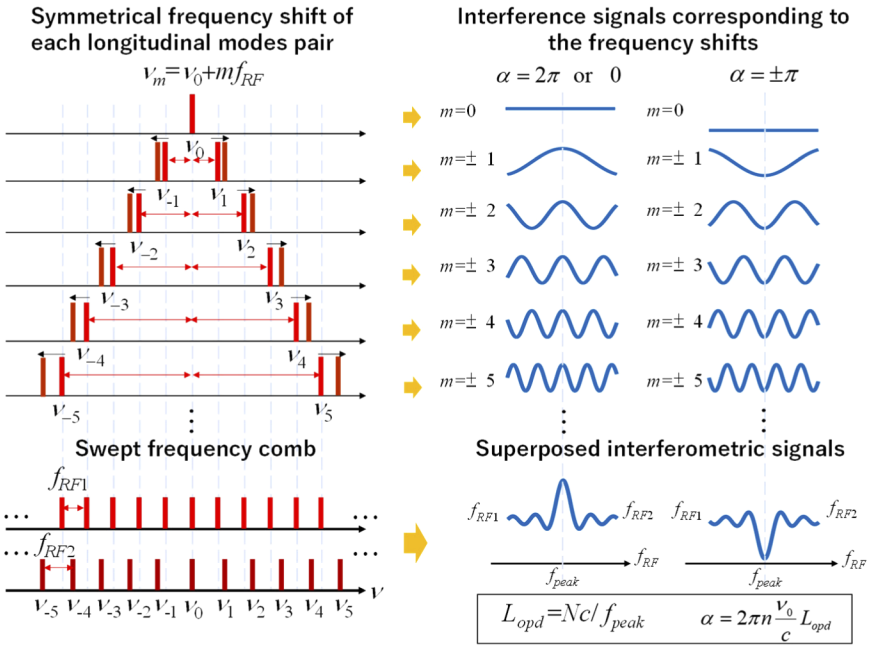

Fig. 1. Principle of the optical comb interferometry. The axisymmetric frequency sweeping produces a phase-sensitive amplitude peak waveform without a fringe in the interferometric measurement. This method measures the OPD as a reflecting position by finding the peak frequency f_{peak}. In addition, the minute displacement resulting from the subtle phase fluctuation can be detected by the change in the amplitude.

In the proposed method, the center frequency ν_0 of the optical comb does not change because it is a continuous wave (CW) component of the seed light source. Therefore, when the modulation frequency of the RF signal is swept, the FS varies with a symmetrical spectral distribution in the positive and negative directions around this CW component, as shown in Fig. 1. Note that the phase $\alpha = 2\pi\nu_0 L_{opd}/c$ is invariant because L_{opd} is fixed during the RF sweeping. Here, $B(f_{RF}, L_{\mathrm{OPD}})$ can be interpreted as the Fourier series expansion for the Fourier coefficient a_m, which is a periodic peak function with repeated peak values at a certain interval of $f_{RF} = c/L_{opd}$ on the f_{RF} axis. For $B(f_{RF})$ to have a maximum value when f_{RF} is swept from f_{RF1} to f_{RF2}, as shown in Fig. 1, the following must hold:

$$\frac{f_{RF}L_{opd}}{c} = N, \tag{3}$$

where N is an integer called the interferometric order. Therefore, if we define the f_{RF} that gives the interference peak as the peak frequency f_{peak}, the OPD of the interferometer can be obtained from this peak frequency as $L_{\mathrm{opt}} = Nc/f_{peak} = L_N$.

In the actual measurement, it is necessary to know the interference order N in advance. Figure 2(A) shows the relationship between L_{OPD} and FS as the peak frequency when $f_{RF} = f_{peak}$. Sweeping the FS f_{RF} from f_{RF1} to f_{RF2} with a sweep range of $\delta f = |f_{RF1} - f_{RF2}|$ is equivalent to scanning a region with an OPD of $\delta L = |L_2 - L_1| = N(c/f_{RF}^2)\delta f$ from $L_2 = Nc/f_{RF2}$ to $L_1 = Nc/f_{RF1}$. The scan range δL for a frequency sweep is proportional to the interferometric order N and inversely proportional to the square of f_{RF}. Figure 2(B) shows the sweep range variation $\delta L/\delta f_{FR}$ for the frequency sweep corresponding to N and f_{RF}. From Eq. (2), when f_{RF} changes near the peak frequency f_{peak}, the N-th order interference signal can be rewritten as follows:

$$I_N(f_{RF}) = I_0 \cos(\alpha) B_N(f_{RF} - f_{peak}), \tag{4}$$

Optics EXPRESS

where I_0 is the amplitude coefficient and B_N is a waveform of the N-th cycle of the periodic function $B(L_{OPD})$ counting from OPD = 0. This waveform is defined as a function such that $B_N(0)$ gives the peak value. The detailed waveform is proportional to the inverse Fourier transform of the total power spectrum of the light sources contributing to the interference, according to the Wiener–Kinchin theorem [27].

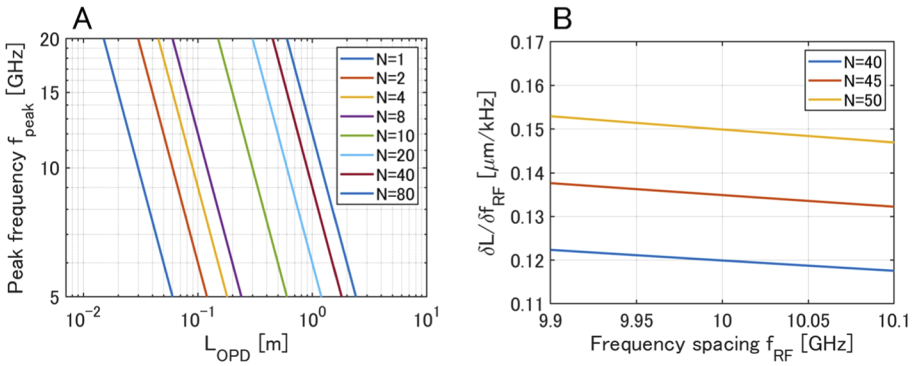

Fig. 2. (A) Relation between the peak frequency f_{peak} and corresponding OPD for various values of interferometric order N. OPD changes proportionally to N but inverse proportionally to f_{peak}. For instance, when f_{peak} is 10 GHz, OPD is N times 30 mm. Here, we assume that the refractive index of the medium is 1. (B) Change in the slope of δL with the frequency sweeping amount δf_{RF} as a function of f_{FR} with different N (40, 45, and 50). The slope slightly disperses inverse proportionally to the square of f_{FR} as the FS is swept.

Because the frequency sweep in this method is performed independently of the fixed ν_0, the amplitude of I_N depends on a fixed value of cos(α), as is clear from Eq. (4) [40]. Therefore, this allows for compressive sensing, where the number of data points used for measurement can be significantly reduced compared to that required by the Nyquist-Shannon sampling theorem for conventional interference fringe measurement, because a peak envelope without fringes will be observed. Furthermore, as shown in Fig. 2, the peak amplitude presents a steep fringe-like change in response to the phaseα, whereas the envelope of B_N is almost invariant to the displacement fluctuation due to small changes in L_{OPD}. By applying this feature, displacements in the vicinity of the reflecting positions of sample surfaces can be detected with nanometer precision.

This phase sensitivity can be understood in relation with the CEO. As a simple example, when the center frequency is equal to an integer multiple of the peak frequency at which the interference peak is observed (i.e., $\nu_0 = p\, f_{peak}$, where p is an integer), the phase becomes an integer multiple of 2π and the amplitude of the peak reaches its maximum value. The phase α_N at the N-th-order peak position can be expressed as follows:

$$\alpha_N = \frac{2\pi\nu_0 L_N}{c} = 2\pi N\left(\frac{\nu_0}{f_{peak}}\right) = 2\pi N\left(\frac{pf_{peak} + f_{CEO}}{f_{peak}}\right) = 2\pi(m + \Delta_N), \tag{5}$$

where f_{CEO} is the CEO frequency, $\Delta_N = Nf_{CEO}/f_{peak}$ denotes the frequency ratio, and N, p, and $m = Np$ are integers. The actual observed phase value α'_N will be wrapped from –π to π rad; hence, it can be expressed as $\alpha'_N = 2\pi\Delta_N$. Furthermore, the exact OPD L_λ using the phase α'_N can be synthesized as follows:

$$L_\lambda = \frac{c\alpha_N}{2\pi\nu_0} = (m + \Delta_N)\lambda = m\lambda + \frac{\alpha'_N}{2\pi}\lambda, \tag{6}$$

where λ is the center wavelength of the optical comb, which is obtained from the CW frequency. In practical measurements, m is estimated by comparing it with L_N obtained from the interference

Optics EXPRESS

peak position. As long as m is estimated accurately, the synthesized distance L_λ can be used to measure the distance with nm accuracy.

2.2. Setup

Figure 3 shows the experimental setup. Because the purpose of this experiment was to confirm the principle, a single-point measurement system without spatial scanning was designed. The measurement system consisted of a light source, interferometer, and detection unit. The light source, consisting of a DD-MZM (OFCG-PS-1550, Sevensix), high-power erbium doped fiber amplifier (EDFA) (AEDFA-33-B-FA, Amonics), and highly nonlinear dispersion-shifted fiber (HN-DCF), emitted a multi-GHz SC comb through a broadening mechanism based on optical nonlinear effects. In this process, the CW light from the laser diode (LD) (AQ2200-136TLS, YOKOGAWA; linewidth < 1 MHz; absolute wavelength accuracy <±100 pm) was first input to the DD-MZM through the optical fiber to generate a 10 GHz spacing comb light (Fig. 4(A)). Next, the comb light was amplified to 33 dBm (24 W) by the high-power EDFA and propagated through the 200 m HN-DCF. Since the zero-dispersion wavelength of HN-DCF was 1.55 µm, the spectrum was broadened relatively flatly through the effects of self-phase modulation and optical parametric amplification [36]. As a result, we generated an SC comb with a bandwidth of approximately 50 nm, as shown in Fig. 4(B). The full-width-at-half-maximum (FWHM) of the coherence function obtained by SC light was approximately 50 µm with a round-trip OPD. The depth resolution of the OCT, defined as the FWHM of the peak waveform obtained by squaring the envelope of this coherence function, was estimated to be 25 µm. As shown in Fig. 4(D), the coherence waveform obtained from the SC comb shows a wide range of ripples around the peak. The intensity ratio between the interference peak and ripple was approximately 30 dB, which caused contrast degradation and false detection in OCT imaging.

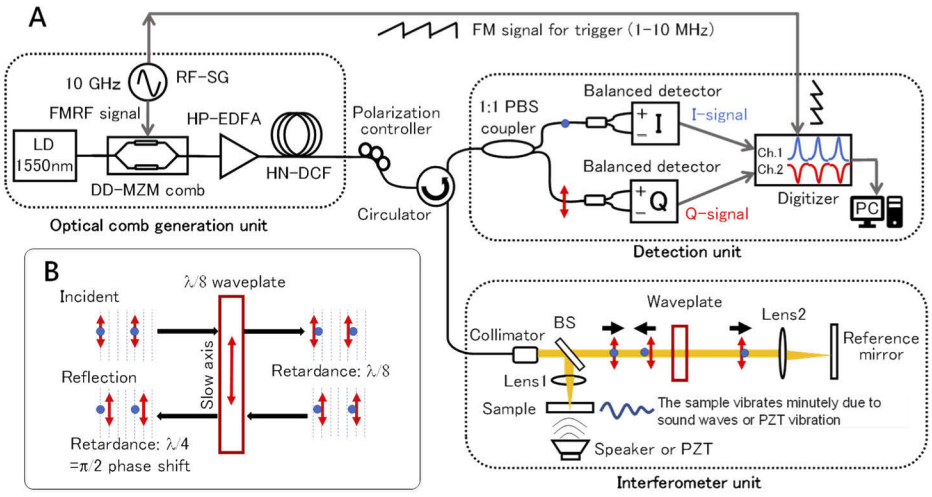

Fig. 3. Experimental setup. (A) Measurement system. (B) Polarization-based demodulation method using a 1/8 wave plate. LD: laser diode; FM: frequency modulation; DD-MZM: dual-drive Mach–Zehnder modulator; RF-SG: radio frequency signal generator; HP-EDFA: high-power Erbium doped fiber amplifier; HN-DCF: highly nonlinear dispersion compensated fiber; PBS: polarization beam splitter; I: in-phase signal; Q: quadrature phase-shifted signal; BS: beam splitter; PZT: piezo-electrical transducer; PC: personal computer.

For a rapid sweep of the FS, the RF signal from a signal generator (SMA 100B, Rohde & Schwarz) was modulated by FM with repetition rates of 1–10 MHz. The FM signal was generated from the local oscillator of the signal generator. The FM frequency deviation was limited to

Optics EXPRESS

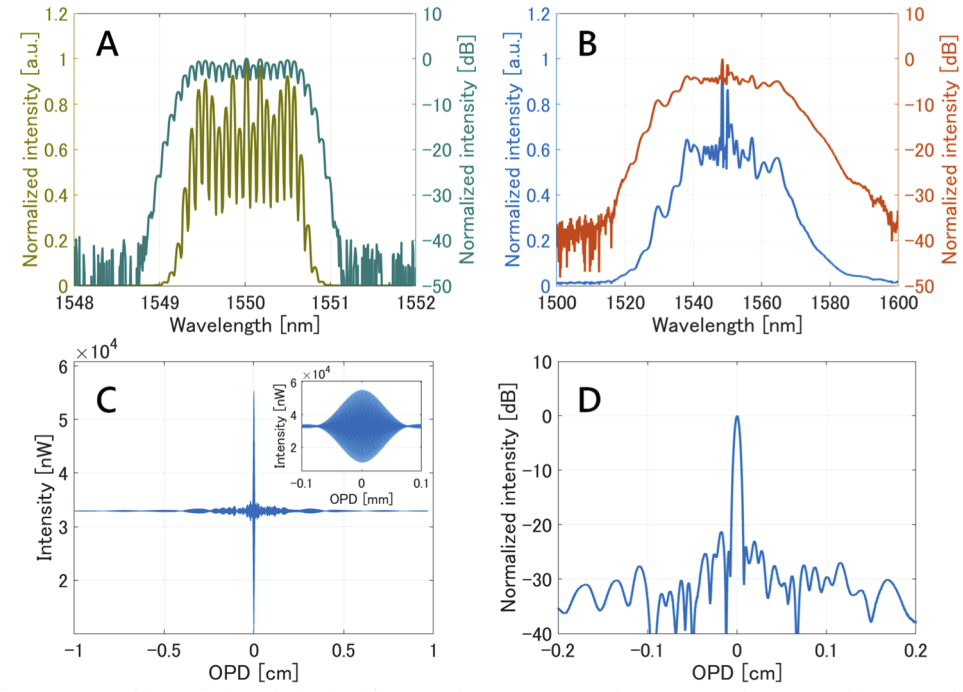

Fig. 4. Spectra of the optical comb obtained from (A) the DD-MZM comb generator and (B) SC multi-GHz comb. A 10 GHZ SC comb with a bandwidth of approximately 40 nm was generated. (C) Coherence function obtained by an interferometric spectrometer from the SC comb of (B). The FWHM of the peak was approximately 70 µm in terms of the round-trip OPD. (D) Waveform plot showing the interferometric peak intensity envelope extracted from (C) on a log scale. The FWHM of the peak envelope was approximately 25 µm.

approximately ±20 MHz, which is within the range that could maintain the RF phase condition for the DD-MZM. As shown in Fig. 2(A), we could expand the measurement range from this limited frequency sweep range using a higher interferometric order signal.

For repetition rates from 1 to 10 MHz, only sinusoidal FM signals were provided. Up to 1 MHz, the FM signal could be generated in the sawtooth waveform, and linear frequency sweeps could be achieved. A maximum scan rate of 20 MHz was achieved because frequency modulation of 10 MHz allowed two round-trip scans in one cycle. Using this method, the relationship between the amount of frequency sweep and the scan range is nonlinear, as shown in Fig. 2.

The interferometer was a fiber optics system with a spatial interferometer. The SC comb light from the light source was linearly polarized by the polarization controller and incident to the spatial interferometer through the circulator. The interferometer was of an unbalanced Michelson type with a long OPD, which interfered with the light waves reflected from the reference mirror and the object. The position of the reference mirror was set in the range of approximately 1200 mm in terms of the OPD to observe interference signals of the interferometric order N of 44 or 45.

For phase retrieval from the interference signal, a waveplate that functions as a 1/8λ plate for a 1.5 mm light wave was inserted on the reference arm. Using this wavelength plate, the phase of the light wave in the slow axis was delayed by π/2 in the round trip compared to that in the fast axis, as shown in Fig. 3(B). In this process, the reflected light from the measurement object and reference mirror interfered and returned to the circulator. Immediately, the interfered light wave was split into S- and P-polarized components by a 1:1 PBS coupler connected to the output port

Optics EXPRESS

of the circulator. The S- and P-polarized interference signals were detected simultaneously and independently by two balanced detectors (PDB 415C, Thorlabs, bandwidth 100 MHz). These fast temporal electrical signals were recorded or observed by a digitizer with two channels of sufficient bandwidth (in the experiments, devices with different sampling rates were used for different purposes). This polarization-based demodulation method instantaneously determines the peak intensity distribution and phase from the acquired interference signal.

As mentioned earlier, the detector detects the signals of two polarization components whose phases are shifted by π/2 from each other. Therefore, by defining the interference signal in the fast axis as in Eq. (5), the polarization component from the other slow axis can be written as

$$Q_N(f_{RF}) = Q_0 \cos(\alpha - \frac{\pi}{2} - \theta)B_1(f_{RF} - f_{peak} - \delta) \approx Q_0 \sin(\alpha - \theta)B_1(f_{RF} - f_{peak}), \quad (7)$$

where θ is defined as the phase shift due to retardation error caused in the 1/8λ plate, and δ is the difference in OPD, which changes slightly due to the phase shift caused by the 1/8λ plate. δ is negligible because it is at most λ/4 (approximately equal to 0.3 μm), which is approximately 0.5% of the OCT resolution of the system. Equations (4) and (7) are defined as I-signal and Q-signal, respectively, where Q_0 denotes the amplitude coefficient of the Q-signal.

Based on the observed I- and Q-signals, the time variation of the interference intensity and phase distribution was investigated by synthesizing a complex interference signal Z as follows:

$$Z(f_{RF}) = \left[\frac{I_N(f_{RF})}{|I_0|} + i\frac{Q_N(f_{RF})}{|Q_0|}\exp(-i\theta)\right]\frac{\exp(i\theta)}{\cos\theta} = \mathrm{Re}[Z(f_{RF})] + i\mathrm{Im}[Z(f_{RF})]. \quad (8)$$

The retardation phase error θ, which varies with the angle of the 1/8λ plate and wavelength of the light wave, must be determined in advance by calibration. In addition, the signal magnitudes $|I_0|$ and $|Q_0|$ must be known before measurement through calibration. In our experiment, we observed the maximum and minimum values of the I- and Q-signals (denoted by I_{max}, Q_{max}, I_{min}, and Q_{min}) by moving the position of the reference mirror attached to a piezoelectric actuator over a distance greater than the wavelength. Then, we obtained these parameters using the equations $|I_0|=(I_{max}-I_{min})/2$ and $|Q_0|=(Q_{max}-Q_{min})/2$. Finally, the phase and peak intensity observed at the N-th order interference signal were retrieved by $\alpha'_N = \tan^{-1}(\mathrm{Im}[Z(f_{peak})]/\mathrm{Re}[Z(f_{peak})])$ and $I_{peak} = |Z(f_{peak})|^2$, respectively.

3. Results

3.1. Tomographic transient displacement measurement

To validate the proposed method, rapid tomographic vibration measurements were conducted on a thin glass film (thickness: 120 μm; tolerance: ±10 μm; refractive index: 1.44) vibrated by sound waves. A speaker was placed behind the thin film at approximately 8 cm to initiate sound wave vibration. The sound stimulation was a 5 kHz amplitude modulated sine wave by a ramp function with a repetition rate of 200 Hz. The average sound pressure level was approximately 100 dB. Figure 5(A) shows the voltage signal applied to the speaker and sound wave waveform recorded by a microphone. To ensure a sufficient measurement range, the reference mirror was placed at a distance of approximately 1320 mm in OPD, where the 44th interferometric order signal could be observed. The FS of the multi-GHz SC comb was swept by frequency modulation of the RF signal with a sawtooth waveform from 9.990 to 10.010 GHz with a deviation of 20 MHz and duration of 1 μs. This sweep resulted in a depth scan of approximately 1.3 mm, ranging from 658.8791 to 660.1981mm at a scan rate of 1 MHz. A digitizer (SA240P, Acqiris, 14 bit) with a sampling rate of 1 GS/s was used to perform 20,000 time-series scans over a period of 20 ms, with a total of 20 million points measured. Thus, we took 1000 data point measurements per scan, and the resolution of the depth profile was approximately 1.3 μm/sample.

Optics EXPRESS

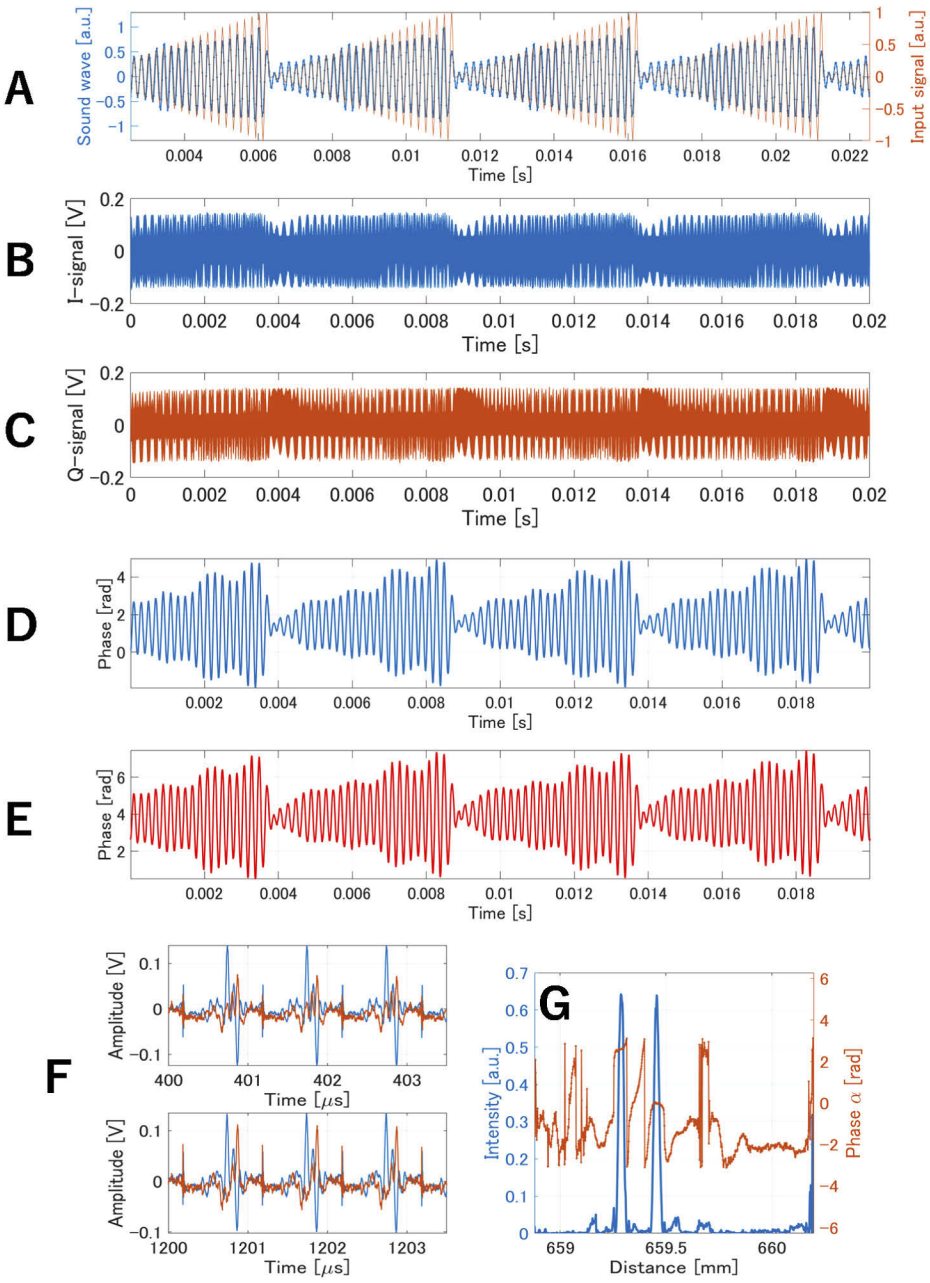

Fig. 5. Measurement results for a thin glass film vibrated by a sound wave. (A) Voltage signal input to a speaker (orange) and sound wave recorded by a microphone (blue). (B) I-signal and (C) Q-signal after applying the noise reduction process. (D and E) Resulting temporal phase changes at the positions of the front and rear surfaces, respectively. (F) Enlarged I-signal (blue) and Q-signal (orange) over two different time ranges. (G) Typical single period signal of the intensity (blue) and phase (orange) distributions utilizing the synthetic complex amplitude signal Z with compensations of the retardation error and amplitude ratio between I/Q signals. These signals were recorded with 1 MHz scan rate and 1 GHz sampling. The periodical dip shown every 1 μs was caused by the rapid change in the amplitude when the swept RF frequency returned to an initial value.

Optics EXPRESS

Figure 5(B and C) shows the resulting interference waveforms of the I- and Q-signals. These signals were denoised using sparsity in the spectral region of the repeated signal as a preprocessing step (see Section 4 for details). The synthetic complex signal Z was generated from these I- and Q-signals according to Eq. (7). In the experiment, $\theta = 0.2$ rad; the ratio of $|I_0|$ to $|Q_0|$ before correction was 100:99.

The interference phase α'_N obtained from the synthetic complex signal Z is shown in Fig. 5(D) and 5(E). With a scan rate of 1 MHz, the transient temporal displacement caused by the sonic vibration of the glass film could be measured along with the reflection positions. It was difficult to make a simple comparison with the sound wave because it changes depending on the position of the microphone, and the elasticity of the glass film causes distortion of the waveform. Nevertheless, from the results, we confirmed that the magnitude changes and phase of the vibration in the ramp shape were roughly consistent. In addition, the interference peak intensity $|Z|^2$ was obtained, and the cross-sectional locations of the front and rear surfaces could be imaged as in OCT, as shown in Fig. 5(G).

Next, the exact reflection position of each interface of the thin glass film was estimated, and the film thickness was derived (Fig. 6). The average reflection positions l_p at the rear and front surfaces, as estimated by the interference intensity peak positions, were $l_{p1} = 659.4438$ mm and $l_{p2} = 659.2668$ mm, respectively. The standard deviations (SDs) of these reflection positions were 4.1597 µm and 4.6618 µm, respectively. From Eq. (6), the average synthesized distances $l_\lambda = L_\lambda/2$ were estimated to be $l_{\lambda1} = 659.4435$ mm and $l_{\lambda2} = 659.2675$ mm, respectively, with SDs of 0.1711µm and 0.1734µm, respectively, using l_{p1} and l_{p2}, measured phase α'_N, and central wavelength $\lambda = 1.5493$ µm measured by a spectrum analyzer. The corresponding m values in Eq. (6) were estimated to be $m = 851290$ and 851063, respectively, as values that gave the minimum of merit functions expressed as $|m\lambda - l_{p1}|$ and $|m\lambda - l_{p2}|$, respectively. According to Fresnel equations, the phase of the optical field shifts by π due to the reflection at the boundary surface where the refractive index changes from high to low, therefore, it is necessary to include this π phase shift in deriving the synthesized distance $l_{\lambda2}$ at the rear surface. Thus, we used the compensated phase $\alpha_{N\pi} = \arg\{exp[i(\alpha'_N - \pi)]\}$ for the estimation of the rear surface position.

Furthermore, the average film thicknesses were obtained from the peak positions l_p and the synthesized distance l_λ. The thickness d_p calculated by $|l_{p1} - l_{p2}|$ was found to be 176.9869 µm on average, with an SD of 4.6356 µm. The film thickness d_λ calculated by $|l_{\lambda1} - l_{\lambda2}|$ was 175.9296 µm on average, with an SD of 0.0123 µm. The estimated film thickness considering the refractive index of 1.4440 from the synthesized distances was 121.8349 µm. This result is reasonable considering the tolerance of ±10 µm for the glass film and the resolution of the measurement system (1.3 µm/sample). Figure 6(C) shows that it is possible to measure the film thickness with nm accuracy from the synthesized distance, even when the glass film oscillates transiently.

Figure 7 shows a tomographic time-lapse image of one cycle of the intensity and phase signal mapped on the vertical axis and displayed chronologically on the horizontal axis, which allows the temporal changes in each scan to be visualized. The phase distribution was replaced with the hue value of the HSV image; the intensity was replaced with the saturation and brightness values. This display method effectively visualizes the temporal changes in the displacement of the µm and nm regions of the cross-section.

3.2. Measurement with 20 MHz scan rate

Next, to verify the fast measurement of the multi-MHz scan rate, the thin glass film used in the previous experiment was attached to a PZT device and subjected to 50 kHz pure tone sinusoidal micro-vibration. The interferometric order was set to 45 on the interferometer, and the same measurement system was used. In this experiment, the frequency of the RF signal was modulated sinusoidally; therefore, two scans (forward and reverse) were performed within one cycle with a duration of 0.1 µs. Because both scans were used for the measurements, the

Optics EXPRESS

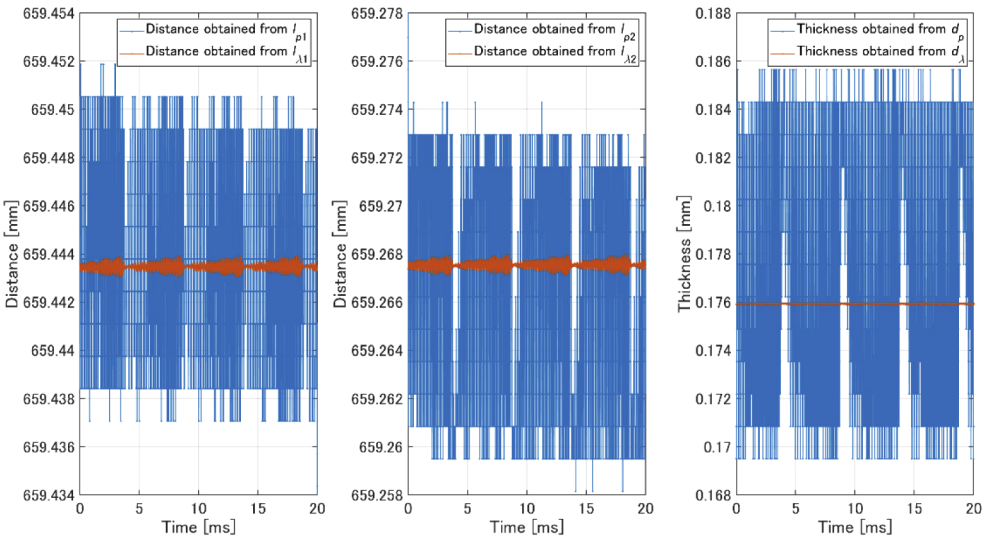

Fig. 6. Comparison of the estimated temporally fluctuating surface positions of the thin glass film based on the peak intensity change (blue) and synthesized distance based on the phase change (orange). (A) Front surface positions. (B) Rear surface positions. (C) Thickness including refractive index $n = 1.444$ calculated by subtracting the distances of (A) from those of (B).

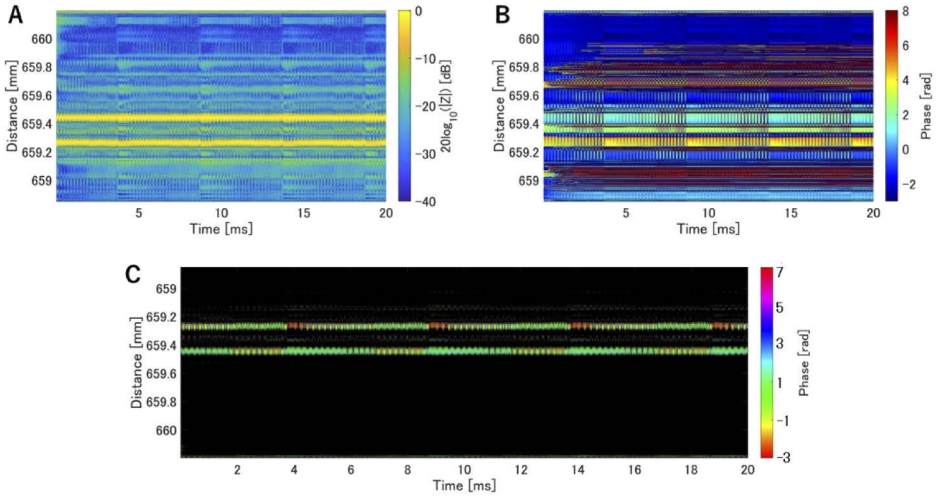

Fig. 7. Tomographic time lapses. (A) Normalized intensity distribution $|Z|^2$. The imaging contrast was set to be 40 dB on a log scale. Note that the interference pedestal regularly appeared approximately –30 dB down around peaks; this was not random noise. (B) Unwrapped phase distribution. (C) Intensity-phase synthetic image made from (A) and (B). The intensity component below –15 dB was eliminated in this image.

Optics EXPRESS

scan rate reached 20 MHz. The frequency deviation was set to 5 MHz, and the sweep range was 9.995–10.005 GHz, resulting in a measurement range of 674.1904 – 674.8649 mm. The measurements were performed at a sampling frequency of 4 GS/s for 0.1 ms, and 2000 A-scans were recorded with a resolution of 200 points resolving a range of 674.4861 µm. Compared to typical time-domain low-coherence interferometry and SS-OCT, the number of pixels was smaller, and a more compressive measurement was conducted. The average resolution was approximately 3.4 µm/sample, which varied with position because of the nonlinear sweep using a sinusoidal wave for the FM.

Figure 8 shows the I- and Q-signals of the thin glass film, where the intensity and phase distributions were generated from the synthetic complex signal Z. As in the analysis of the previous section, Figs. 9(A) and 9(B) show the tomographic time-lapse images of the forward and reverse scans. As shown in Figs. 9(C) and 9(D), the micro displacements at each interface obtained from the synthesized distance L_λ show oscillations of approximately 80 – 100 nm in amplitude at 50 kHz. The film thickness measured by the forward scan had a mean value of 0.1746mm with an SD of 0.0148 µm. Similarly, the thickness measured by the reverse scan had a mean value of 0.1746mm and SD of 0.0139 µm. There was a difference of approximately 3 µm from the film thickness obtained in the previous experiment. This difference is due to the different location of the measured position and the resolution per pixel. The same level of thickness fluctuation was observed in the measurement with a 20 MHz scan rate.

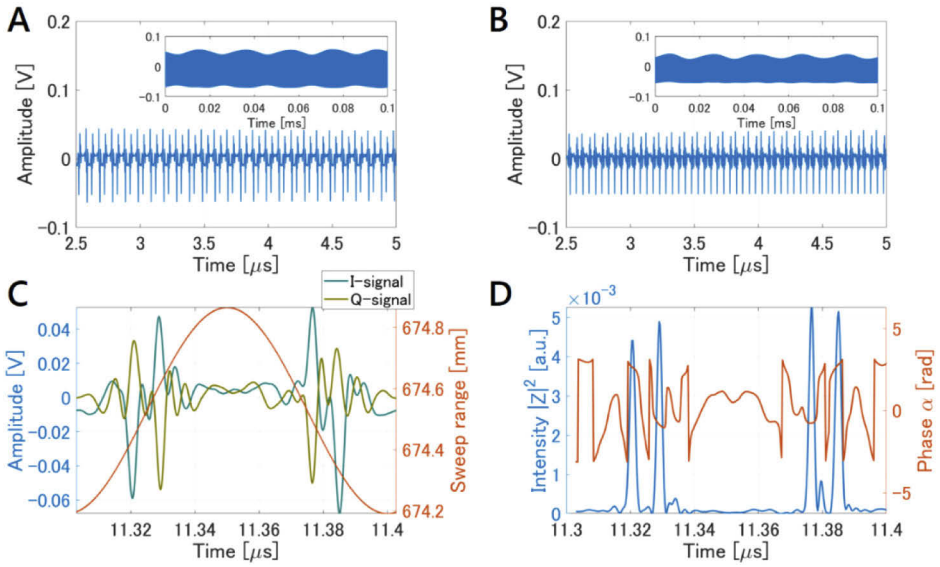

Fig. 8. Acquired data utilizing RF frequency sweep with 10 MHz sinusoidal FM. (A) I-signal. (B) Q-signal. (C) A single period of I/Q-signals with scan range. The sinusoidal RF sweeping provided a round trip ranging with forward and reverse directions during one period, which achieved a 20 MHz scan rate.

The results of the forward and reverse scans are not in perfect agreement with each other. There is a difference of a few nanometers between the two results. The reason for this discrepancy may be due to the fluctuation of the optical comb's central wavelength during the 0.05 ms between one scan and the next as well as the asymmetry caused by the error and noise in the sinusoidal RF scan signal. In addition, 10 MHz scan rate measurements are not suitable for precise position identification because the resolution of the measurement points is limited due to the limited sampling rate. Nevertheless, by extracting the interference phase from calculating the synthesized

Optics EXPRESS

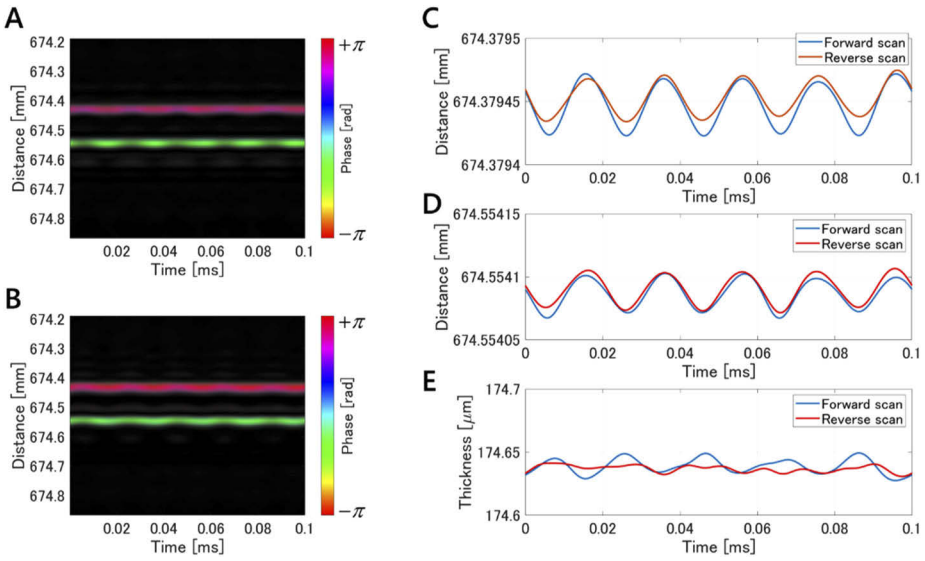

Fig. 9. Measurement results of the vibrating thin glass film with 20 MHz scan rate. (A) and (B) show the tomographic time-lapse images utilizing forward and reverse scans, respectively. The contrast of these images was set to 10 dB. (C) and (D) show the temporal displacements at the front and rear surfaces, respectively, which were estimated from each synthesized distance. (E) Thickness estimated by subtracting the displacement (C) from (D).

distance, it was shown that fast displacement measurement at each peak position beyond the OCT depth resolution could be possible with an accuracy of 10–20 nm.

3.3. *Vibration measurement for a PZT surface*

Next, we measured the surface vibration of a PZT (PC4QR, Thorlabs) device to investigate the tracking ability against frequency in vibration measurement. A sinusoidal voltage signal with a frequency of 10 to 100 kHz and amplitude of 20 Vpp was applied to the PZT to generate micro-vibrations. The RF signal corresponds to a measurement range of 674.1904–674.8649 mm in the sweep range of 9.995–10.005 GHz, as in the settings of the previous section. The RF frequency was also swept sinusoidally at a round-trip 20 MHz scan rate, as described in the previous section. An 8-bit data acquisition (DAQ) interface (PXI-5154, National Instruments; sampling rate 1 GS/s) was used as a digitizer because the main purpose of this experiment was to detect the phase of the surface profile. To detect the phase change of the PZT surface, 5000 scans were performed over 0.5 ms. Figure 10 shows the results of vibration analysis of the PZT for vibration from 10 to 100 kHz. The phase distribution of the interference peak position was extracted from the Z-signal using the same method as described earlier. The dynamic time variation of the phase is shown in Fig. 10(A). The resulting power spectra obtained by fast Fourier transform (FFT) analysis for each frequency are shown in Figs. 10(B) and 10(C). Each measured frequency component matched the vibration frequency of the PZT. In the analysis, signals above 450 kHz were cut off due to the filtering bandwidth used in the signal denoising process (see Section 4). The mean + 2×SD values of the vibration amplitude calculated from the noise floor in the high frequency range without interference signals were estimated to be approximately 1.0 (mean: 0.5 nm; SD: 0.25 nm) and 0.9 nm (mean: 0.4 nm; SD: 0.25 nm) for the forward and reverse scans, respectively. These values are the minimum detectable amplitudes, which are defined as the vibration measurement sensitivities of our system.

Optics EXPRESS

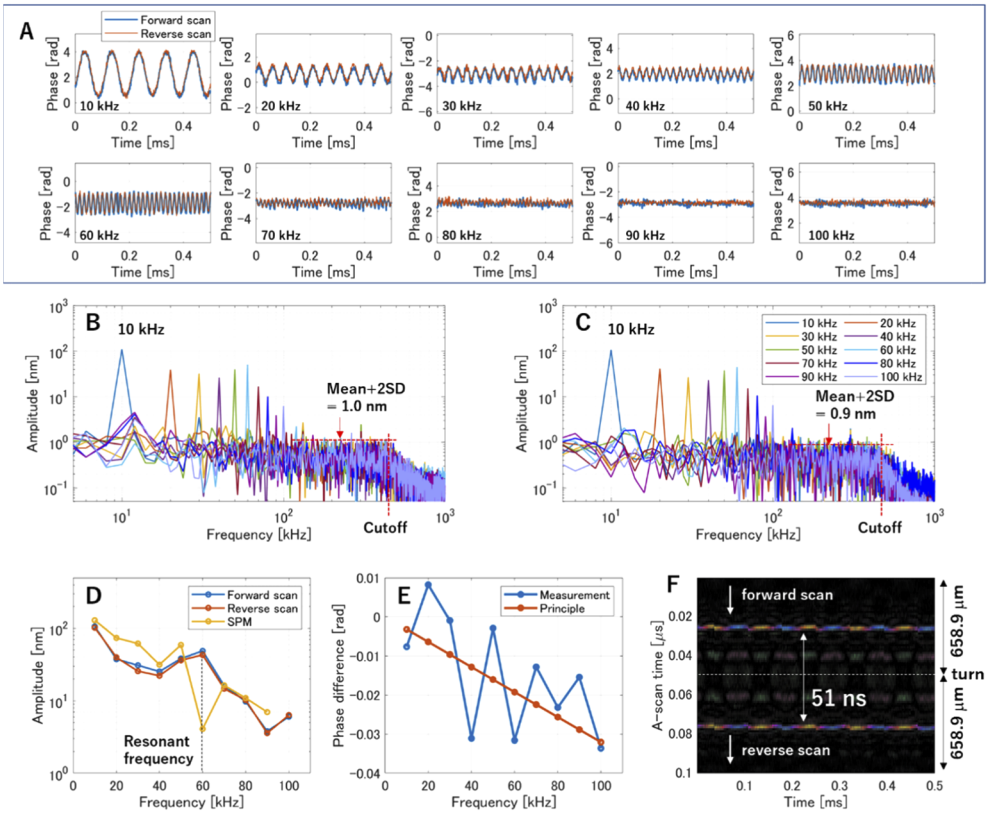

Fig. 10. Vibration analysis of a PZT for the frequency change. (A) Dynamic measurements of the PZT surface displacement in terms of the temporal interferometric phase change. (B, C) Frequency analysis utilizing FFT of each temporal displacement with different frequency (10–100 kHz) obtained by the (B) forward and (C) reverse scan. (D) Vibration amplitude as a function of the frequency applied to the PZT, where SPM represents modified sinusoidal phase modulation laser interferometer. (E) Phase difference between forward and reverse scanning at each intensity peak frequency. (F) Tomographic time-lapse image of the PZT surface displacement without separating the forward and reverse scans. The HSV color represents the phase value in the same manner as in Fig. 7(C).

Optics EXPRESS

The vibration amplitude changes for each frequency, estimated from the peak intensity values, are shown in Fig. 10(D). The mean difference between the measured vibration amplitude values in the forward and reverse scans was 2.4 nm with an SD of 2.6 nm. Furthermore, we examined the validity of the measurements by comparing them with those obtained by a different method, the modified sinusoidal phase modulation (SPM) lase interferometer [41]. At a frequency of 60 kHz, which is near the resonance frequency of the PZT used, the amplitude values measured by the SPM laser interferometer differed significantly from the experimental values, while similar trends were observed at other frequencies. Owing to the bandwidth limitation of the SPM laser interferometer, a comparison at 100 kHz was not possible. Regarding this discrepancy, it should be considered that the same PZT was not under exactly the same conditions because of changes in the actual applied voltage value and impedance.

The difference between the phase values of the vibration at each frequency obtained by the forward and reverse scans is shown in Fig. 10(E). Because the RF frequency is swept in the time domain, there is a time difference between the distributions obtained by the forward and reverse scans. This difference represents the time lag of the phase caused by the scan time delay. The time spent in one scan is determined by the scan rate, which is 0.1 μs at 10 MHz. Considering a round trip, one depth scan will have a time difference of 0.05 μs. The phase delay depends on the oscillation frequency of the sample. In this experiment, the theoretical phase delay calculated from the vibration period of the PZT plane and scan time was 3.2 mrad/kHz. The SD of the difference between the theoretical and experimental phase delay for each frequency was 11.4 mrad. It was confirmed that the phase delay due to the scan time difference could be detected with a sub-10 mrad accuracy. Therefore, this method can determine the exact phase at the time of scanning at the reflection position. Such a time-reserved method will be useful for detecting faster and finer phase changes. The experimental results show that the proposed method has potential applications in the analysis of transient motion and frequency response as well as determining the shape of vibrating objects that vibrate at high speed, such as PZTs and MEMSs.

4. Discussion

4.1. Noise reduction

The proposed method has the three advantages of compressive sensing, free manipulation of measurement range, and multi-MHz scan rate, which are difficult to achieve with conventional OCT. Nonetheless, studies on OCT sensitivity have shown that FD-OCT is superior to TD-OCT in terms of the number of pixels used for imaging [42–44]. The sensitivity limitation of TD-OCT is mainly due to the wide electrical band width caused by the low coherence of the temporal signal, which is photoelectrically converted at the detector [42,44]. The sensitivity of the proposed method is also expected to be inferior to that of FD-OCT because of the time domain low-coherence peak signals recorded at the detector.

Notwithstanding this, our method can enhance the sensitivity of conventional TD-OCT through noise reduction by signal processing using discrete Fourier transform (DFT) and frequency filtering because multiple repetitive signals are detected owing to the fast sweeping of the optical comb (Fig. 11). The DFT of the repetitive signal obtained by FM sweeping of the RF gives an equispaced comb waveform with sidebands in the Fourier domain. The overall intensity envelope of this spectral domain comb originates from the waveform of the Fourier transform of the interference peak function, and the sidebands around each comb component originate from a function of the temporal variation of the repetitive signal, i.e., the displacement of the measurement object. This comb component is a delta-functional sparse signal with a narrow linewidth. By applying a transmission filter with equispaced FS, i.e., a “comb filter”, on a computer, we can remove the extra noise by passing only the comb component and its sideband related to the interference, as shown in Fig. 11. As a result, the electrical bandwidth consumed by the TD-OCT signal in the detector can be narrowed by exploiting the sparsity in the frequency

Optics EXPRESS

domain. Applying inverse DFT (IDFT) to this thinned signal back to the time domain, we can obtain a higher sensitivity than the original signal. All the results reported for this experiment were preprocessed by noise reduction.

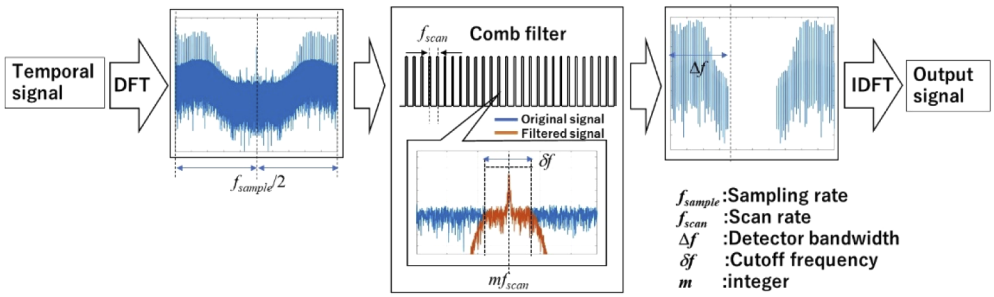

Fig. 11. Schematic of the noise reduction process. The spectrum of the acquired temporal signal was filtered out by a comb filter with an equispaced FS equal to the scan rate. Noise components not involved in the interference were removed. The bandwidth δf of each comb component is a cutoff range that covers the frequency band with a sufficiently short time resolution to detect the vibration or transient displacement of the object.

Figure 12 shows the noise reduction results for the actual measured signal. The noisy signal from the PZT rough surface was recorded with an 8-bit DAQ interface. The noise reduction improved the sensitivity of the vibrational phase change detection by a factor of two compared to the original signal. As shown in Fig. 12(D), the sensitivity defined by the mean + 2×SD value of the noise floor in the frequency domain was 3.4 nm (mean: 1.8 nm; SD: 0.3 nm) for the original signal, which improved to 0.9 nm (mean: 0.5 nm; SD: 0.2 nm) after noise reduction. This result demonstrates the usefulness of noise reduction but does not define the limit of the performance of our method. The sensitivity of this system may be improved from the current level by improving the interferometer and performance of the wavelength stability of the LDs used.

The current resolution of tomographic imaging using the proposed system is inferior to that of conventional OCT, which limits its application to tomographic vibration measurement of simple structures rather than that of biological tissue at this stage. For high-resolution OCT measurement, further broadening of the SC combs is necessary. An ultra-broadening technology for a multi-GHz comb has already been established using nonlinear fibers [45], and further development will enable us to improve the resolution by applying these techniques. In addition, the signal-to-noise ratio (SNR) in biological tissues is further lower than that of glass films or PZT rough surfaces. The sensitivity (i.e. precision) of the vibration measurement also depends on the SNR of the system. Hence, improvement of the SNR of the coherence signal is mandatory for the application to biological measurement. In the current system, the SNR was limited to approximately 30 dB due to the ripple of the interference peak waveform, as shown in Fig. 4(D). For future development, it is desirable to re-shape the spectral profile of the SC comb using a tunable filter and to introduce a stabilized laser source with higher coherence.

4.2. Demodulation error

An issue unique to this method is the demodulation error of the interference amplitude and phase. In the method of demodulating the intensity and phase using the I/Q-signals, the retrieved results contain errors, even after applying compensation for the retardation of the waveplate and amplitude ratio between the two signals.

We investigated the error in the retrieved intensity and phase caused by the retardation correction error $\delta\theta$ and adjustment error of the amplitude ratio R by simulation (Fig. 13). The amplitude ratio was defined as $R = |\mathrm{Re}[Z(f_{RF})]|/|\mathrm{Im}[Z(f_{RF})]|$ for the corrected I- and Q-signals in

Optics EXPRESS

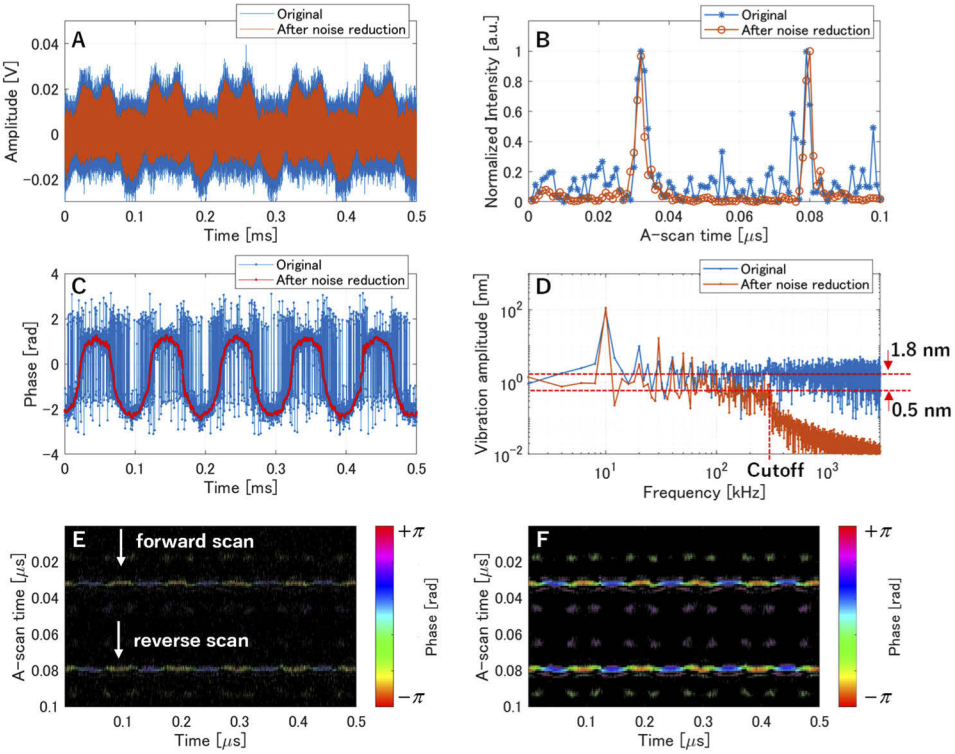

Fig. 12. Results of the noise reduction process. Comparisons of the original and processed (A) temporal interferometric signals from a vibrating surface with a frequency of 10 kHz, (B) intensity peaks for a single cycle obtained from $|Z|^2$, (C) resulting temporal phase changes due to object vibration, and (D) FFT spectral signals of the phase changes. The noise floor of the spectrum was suppressed by the noise reduction process, and the sensitivity of vibration amplitude was consequently enhanced. (E) and (F) show the synthetic time-lapse images with a contrast of 10 dB before and after the noise reduction process, respectively.

Eq. (8). In the simulation, the intensity and phase error rates were defined and evaluated as $\{(|Z_0|^2 - |Z_\varepsilon|^2)/|Z_0|^2\}$ and $\arg[\exp i\{\tan^{-1}(\mathrm{Im}[Z_0]/\mathrm{Re}[Z_0]) - i\tan^{-1}(\mathrm{Im}[Z_\varepsilon]/\mathrm{Re}[Z_\varepsilon])\}]/2\pi$, respectively, where Z_ε is the signal with error added, and Z_0 is the ideal signal without error. In addition, we evaluated the maximum value of the error in all ranges $0<\alpha<2\pi$ because the errors vary with the initial phase α, as shown in the simulation results in Figs. 13(A)–13(D). Figures 13(E) and 13(F) show the distribution of the maximum error rates of the intensity and phase as contour lines as functions of $\delta\theta$ and R for the full range of α. It is suggested that the error rate of the intensity is much worse than that of the phase for the same level of error with $\delta\theta$ and R. To keep the phase error rate within 5%, R and $\delta\theta$ must be adjusted in the ranges of 0.8 to 1.2 and –0.3 to +0.3, respectively. Meanwhile, the intensity error rate was more than 50% for the same error range. Therefore, the phase retrieval is relatively accurate even when the interference intensity demodulation contains considerable error. Because the intensity error rate is prone to degradation, precise adjustment of the retardation and amplitude ratio is necessary to accurately detect tomographic structures by cross-sectional imaging similar to OCT techniques.

Optics EXPRESS

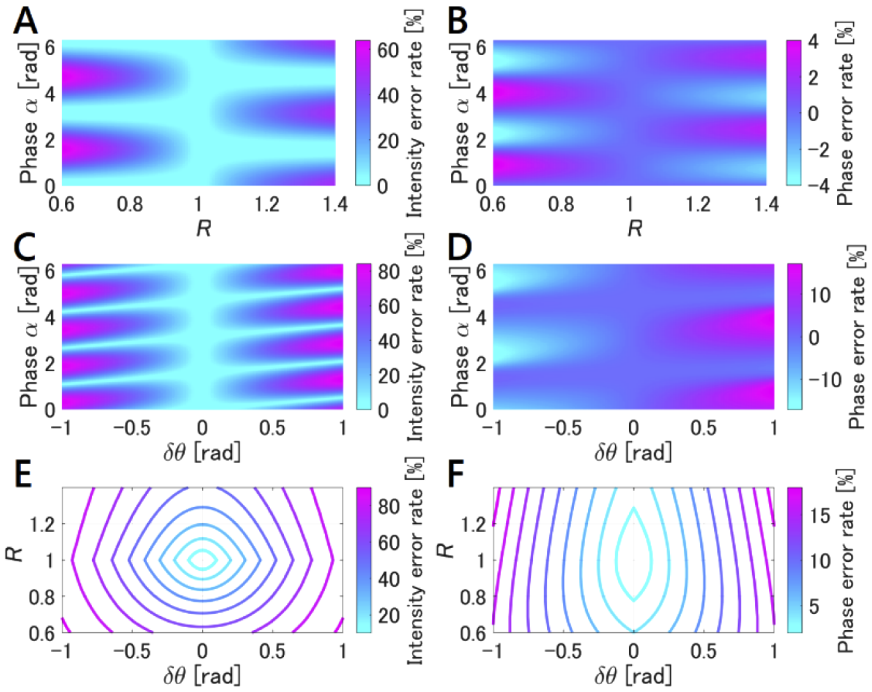

Fig. 13. Simulation results for the demodulation error of interferometric intensity and phase. (A) Intensity error rate as a function of α and R. (B) Phase error rate as a function of α and R. (C) Intensity error rate as a function of α and $\delta\theta$. (D) Phase error rate as a function of α and θ. (E) and (F) show contour graphs of maximum intensity and phase error rates, respectively, as functions of R and $\delta\theta$.

5. Summary

In this paper, we proposed a high-speed tomographic vibration measurement technique using optical combs to measure the tomographic vibration distribution in objects at high frequencies up to ultrasonic. Proof-of-principle experiments demonstrate measurements of transient displacements of a 0.12 mm thick glass film stimulated by sound waves and of a PZT surface vibrating at 10–100 kHz. With this method, we achieved a maximum scan rate of 20 MHz by sweeping a sinusoidal FM-RF signal in the frequency range of 1–10 MHz and tomographic displacement measurements with a depth resolution of 25 µm and sensitivity of approximately 1.0 nm up to a vibration frequency of 100 kHz. For the proposed method to be applied to OCT for biomedical applications, further broadening of the SC optical bandwidth is required. However, the results of this study demonstrate the potential application of a new method using a fast sweep of the optical comb for high-speed cross-sectional displacement imaging and measurement with nanometer accuracy.

Funding. Japan Agency for Medical Research and Development (JP20gm0810004); Japan Society for the Promotion of Science (JP18H02950, JP19H02151, JP20K2016, JP20K21883); Shimadzu; Toray Industries (No. 20-6109).

Acknowledgments. We gratefully acknowledge the support from Prof. Yosuke Tanaka at Tokyo University of Agriculture and Technology and our critical discussion with Prof. Osami Sasaki at Niigata University.

Disclosures. The authors declare no conflicts of interest.

Data availability. Data underlying the results presented in this paper are available in Ref. [46].

Optics EXPRESS

References

1. V. Westphal, S. Yazdanfar, A. M. Rollins, and J. A. Izatt, "Real-time, high velocity-resolution color Doppler optical coherence tomography," Opt. Lett. **27**(1), 34–36 (2002).
2. R. Huber, D. C. Adler, and J. G. Fujimoto, "Buffered Fourier domain mode locking: Unidirectional swept laser sources for optical coherence tomography imaging at 370,000 lines/s," Opt. Lett. **31**(20), 2975–2977 (2006).
3. G. Liu, A. J. Lin, B. J. Tromberg, and Z. Chen, "A comparison of Doppler optical coherence tomography methods," Biomed. Opt. Express **3**(10), 2669–2680 (2012).
4. S. S. Gao, R. Wang, P. D. Raphael, Y. Moayedi, A. K. Groves, J. Zuo, B. E. Applegate, and J. S. Oghalai, "Vibration of the organ of Corti within the cochlear apex in mice," J. Neurophysiol. **112**(5), 1192–1204 (2014).
5. S. S. Gao, P. D. Raphael, R. Wang, J. Park, A. Xia, B. E. Applegate, and J. S. Oghalai, "In vivo vibrometry inside the apex of the mouse cochlea using spectral domain optical coherence tomography," Biomed. Opt. Express **4**(2), 230–240 (2013).
6. H. Y. Lee, P. D. Raphael, J. Park, A. K. Ellerbee, B. E. Applegate, and J. S. Oghalai, "Noninvasive in vivo imaging reveal differences between tectorial membrane and basilar membrane raveling waves in the mouse cochlea," Proc. Natl. Acad. Sci. U. S. A. **112**(10), 3128–3133 (2015).
7. J. Park, J. T. Cheng, D. Ferguson, G. Maguluri, E. W. Chang, C. Clancy, D. J. Lee, and N. Iftimia, "Investigation of middle ear anatomy and function with combined video otoscopy-phase sensitive OCT," Biomed. Opt. Express **7**(2), 238–250 (2016).
8. W. Kim, S. Kim, S. Huang, J. S. Oghalai, and B. E. Applegate, "Picometer scale vibrometry in the human middle ear using a surgical microscope based optical coherence tomography and vibrometry system," Biomed. Opt. Express **10**(9), 4395–4410 (2019).
9. D. MacDougall, J. Farrell, J. Brown, M. Bance, and R. Adamson, "Long-range, wide-field swept-source optical coherence tomography with GPU accelerated digital lock-in Doppler vibrography for real-time, in vivo middle ear diagnostics," Biomed. Opt. Express **7**(11), 4621–4635 (2016).
10. T. Ren, W. He, and D. Kemp, "Reticular lamina and basilar membrane vibrations in living mouse cochleae," Proc. Natl. Acad. Sci. U. S. A. **113**(35), 9910–9915 (2016).
11. C. Rembea and A. Dräbenstedtb, "Laser-scanning confocal vibrometer microscope: Theory and experiments," Rev. Sci. Instrum. **77**(8), 083702 (2006).
12. M. Schnell, P. S. Carney, and R. Hillenbrand, "Transient vibration imaging with time-resolved synthetic holographic confocal microscopy," Opt. Express **26**(20), 26688–26699 (2018).
13. K. Goda, K. K. Tsia, and B. Jalali, "Serial time-encoded amplified imaging for real-time observation of fast dynamic phenomena," Nature **458**(7242), 1145–1149 (2009).
14. D. Choi, H. Hiro-Oka, H. Furukawa, R. Yoshimura, M. Nakanishi, K. Shimizu, and K. Ohbayashi, "Fourier domain optical coherence tomography using optical demultiplexers imaging at 60,000,000 lines/s," Opt. Lett. **33**(12), 1318–1320 (2008).
15. D. H. Choi, H. Hiro-Oka, K. Shimizu, and K. Ohbayashi, "Spectral domain optical coherence tomography of multi-MHz A-scan rates at 1310 nm range and real-time 4D-display up to 41 volumes/second," Biomed. Opt. Express **3**(12), 3067–3086 (2012).
16. W. Wieser, B. R. Biedermann, T. Klein, C. M. Eigenwillig, and R. Huber, "Multi-Megahertz OCT: High quality 3D imaging at 20 million A-scans and 4.5 GVoxels per second," Opt. Express **18**(14), 14685–14704 (2010).
17. S. Moon and D. Y. Kim, "Ultra-high-speed optical coherence tomography with a stretched pulse supercontinuum source," Opt. Express **14**(24), 11575–11584 (2006).
18. K. Goda, A. Fard, O. Malik, G. Fu, A. Quach, and B. Jalali, "High-throughput optical coherence tomography at 800 nm," Opt. Express **20**(18), 19612–19617 (2012).
19. J. Xu, X. Wei, L. Yu, C. Zhang, J. Xu, K. Wong, and K. Tsia, "High-performance multi-megahertz optical coherence tomography based on amplified optical time-stretch," Biomed. Opt. Express **6**(4), 1340–1350 (2015).
20. S. Tozburun, C. Blatter, M. Siddiqui, E. F. J. Meijer, and B. J. Vakoc, "Phase-stable Doppler OCT at 19 MHz using a stretched-pulse mode-locked laser," Biomed. Opt. Express **9**(3), 952–961 (2018).
21. N. Lippok, B. E. Bouma, and B. J. Vakoc, "Stable multi-megahertz circular-ranging optical coherence tomography at 1.3 µm," Biomed. Opt. Express **11**(1), 174–185 (2020).
22. M. Siddiqui, A. S. Nam, S. Tozburun, N. Lippok, C. Blatter, and B. J. Vakoc, "High-speed optical coherence tomography by circular interferometric ranging," Nat. Photonics **12**(2), 111–116 (2018).
23. J. R. Stroud, L. Liu, S. Chin, T. D. Tran, and M. A. Foster, "Optical coherence tomography using physical domain data compression to achieve MHz A-scan rates," Opt. Express **27**(25), 36329–36339 (2019).
24. Y. Ling, W. Meiniel, R. Singh-Moon, E. Angelini, J. Olivo-Marin, and C. P. Hendon, "Compressed sensing-enabled phase-sensitive swept-source optical coherence tomography," Opt. Express **27**(2), 855–871 (2019).
25. K. Liang, O. O. Ahsen, Z. Wang, H. Lee, W. Liang, B. M. Potsaid, T. Tsai, M. G. Giacomelli, V. Jayaraman, H. Mashimo, X. Li, and J. G. Fujimoto, "Endoscopic forward-viewing optical coherence tomography and angiography with MHz swept source," Opt. Lett. **42**(16), 3193–3196 (2017).
26. S. Makita, Y. Hong, M. Yamanari, T. Yatagai, and Y. Yasuno, "Optical coherence angiography," Opt. Express **14**(17), 7821–7840 (2006).
27. S. Choi, M. Yamamoto, D. Moteki, T. Shioda, Y. Tanaka, and T. Kurokawa, "Frequency-comb-based interferometer for profilometry and tomography," Opt. Lett. **31**(13), 1976–1978 (2006).

Optics EXPRESS

28. S. Choi, T. Shioda, Y. Tanaka, and T. Kurokawa, "Frequency-comb-based interference microscope with a line-type image sensor," Jpn. J. Appl. Phys. **46**(10A), 6842–6847 (2007).
29. S. Choi, K. Kasiwagi, Y. Kasuya, S. Kojima, T. Shioda, and T. Kurokawa, "Multi-gigahertz frequency comb-based interferometry using frequency-variable supercontinuum generated by optical pulse synthesizer," Opt. Express **20**(25), 27820–27829 (2012).
30. S.-J. Lee, B. Widiyatmoko, M. Kourogi, and M. Ohtsu, "Ultrahigh scanning speed optical coherence tomography using optical frequency comb generators," Jpn. J. Appl. Phys. **40**(Part 2, No. 8B), L878–L880 (2001).
31. S. Kray, F. Spöler, T. Hellerer, and H. Kurz, "Electronically controlled coherent linear optical sampling for optical coherence tomography," Opt. Express **18**(10), 9976–9990 (2010).
32. J. Kang, P. Feng, B. Li, C. Zhang, X. Wei, E. Y. Lam, K. K. Tsia, and K. K. Y. Wong, "Video-rate centimeter-range optical coherence tomography based on dual optical frequency combs by electro-optic modulators," Opt. Express **26**(19), 24928–24939 (2018).
33. S. Boudreau and J. Genest, "Range-resolved vibrometry using a frequency comb in the OSCAT configuration," Opt. Express **22**(7), 8101–8113 (2014).
34. E. L. Teleanu, V. Durán, and V. Torres-Company, "Electro-optic dual-comb interferometer for high-speed vibrometry," Opt. Express **25**(14), 16427–16436 (2017).
35. S. Choi, N. Tamura, K. Kashiwagi, T. Shioda, Y. Tanaka, and T. Kurokawa, "Supercontinuum comb generation using optical pulse synthesizer and highly nonlinear dispersion-shifted fiber," Jpn. J. Appl. Phys. **48**(9), 09LF01 (2009).
36. B. Xu, X. Fan, S. Wang, and Z. He, "Broadband and high-resolution electro-optic dual-comb interferometer with frequency agility," Opt. Express **27**(6), 9266–9275 (2019).
37. T. Sakamoto, T. Kawanishi, and M. Izutsu, "Asymptotic formalism for ultraflat optical frequency comb generation using a Mach-Zehnder modulator," Opt. Lett. **32**(11), 1515–1517 (2007).
38. A. Parriaux, K. Hammani, and G. Millot, "Electro-optic frequency combs," Adv. Opt. Photonics **12**(1), 223–287 (2020).
39. S. Choi, K. Kashiwagi, S. Kojima, Y. Kasuya, and T. Kurokawa, "Two-wavelength multi-gigahertz frequency comb-based interferometry for full-field profilometry," Appl. Phys. Express **6**(10), 106601 (2013).
40. S. Choi, R. Sato, H. Kato, O. Sasaki, and T. Suzuki, "Multi-frequency scanning interferometry using variable spatial spectral filter," Opt. Commun. **316**, 168–173 (2014).
41. T. Ota, F. Nin, S. Choi, S. Muramatsu, S. Sawamura, G. Ogata, M. P. Sato, K. Doi, T. Tsuji, S. Kawano, T. Reichenbach, and H. Hibino, "Characterisation of the static offset in the travelling wave in the cochlear basal turn," Pfluegers Arch. **472**(5), 625–635 (2020).
42. J. F. de Boer, B. Cense, B. H. Park, M. C. Pierce, G. J. Tearney, and B. E. Bouma, "Improved signal-to-noise ratio in spectral-domain compared with time-domain optical coherence tomography," Opt. Lett. **28**(21), 2067–2069 (2003).
43. R. Leitgeb, C. K. Hitzenberger, and A. F. Fercher, "Performance of fourier domain vs. time domain optical coherence tomography," Opt. Express **11**(8), 889–894 (2003).
44. M. Wojtkowski, "High-speed optical coherence tomography: basics and applications," Appl. Opt. **49**(16), D30–D61 (2010).
45. K. Kashiwagi, T. Kurokawa, Y. Okuyama, T. Mori, Y. Tanaka, Y. Yamamoto, and M. Hirano, "Direct generation of 12.5-GHz-spaced optical frequency comb with ultrabroad coverage in near-infrared region by cascaded fiber configuration," Opt. Express **24**(8), 8120–8131 (2016).
46. S. Choi, "Rapid tomographic vibrometry I/Q signals," *figshare* (2021), https://doi.org/10.6084/m9.figshare.14273342